

EXCITATION CROSS SECTION MEASUREMENT FOR $n = 3$ TO $n = 2$ LINE EMISSION IN Fe^{20+} TO Fe^{23+}

H. CHEN, P. BEIERSDORFER, AND J. H. SCOFIELD

High Temperature and Astrophysics Division, Lawrence Livermore National Laboratory, 7000 East Avenue, Livermore, CA 94551

G. V. BROWN¹

Department of Physics and Astronomy, The Johns Hopkins University, Baltimore, MD 21218

K. R. BOYCE, R. L. KELLEY, C. A. KILBOURNE, AND F. S. PORTER

NASA Goddard Space Flight Center, Code 680, Greenbelt, MD 20771

AND

M. F. GU AND S. M. KAHN

Physics Department, Stanford University, 382 Via Pueblo Mall, Stanford, CA 94305

Received 2004 August 18; accepted 2004 September 23

ABSTRACT

Electron impact excitation cross sections have been measured for iron L-shell $3 \rightarrow 2$ lines of Fe xxI to Fe xxIV at the EBIT-II electron beam ion trap using a crystal spectrometer and a 6×6 element array microcalorimeter. The cross sections were determined by direct normalization to the well-established cross section of radiative electron capture, and a summary of calculated energy-dependent radiative recombination cross sections for electron capture into the $n = 2$ state fine-structure levels of Fe^{16+} to Fe^{23+} ions is given. The measurement results for 17 lines and their comparison with model calculations are presented. While agreement of the model calculations with the experiment is good for most measured lines, significant discrepancies were found for a few lines, including the strongest line in Fe xxI.

Subject headings: atomic data — atomic processes — methods: laboratory — X-rays: general

1. INTRODUCTION

Accurate atomic data are important for the modeling of observed line intensities and for deriving the plasma conditions that are critical in the interpretation of astrophysical observations (Kahn & Liedahl 1990; Paerels & Kahn 2003). Particularly, the atomic data of iron are crucial for interpreting virtually all types of observations, since iron is the most abundant high- Z element. As a matter of fact, the spectra-rich iron L shell has been one of the primary aims of the high-resolution instruments on the *XMM-Newton* and *Chandra* X-ray observatories. Observations with these spacecraft are able to resolve many individual spectral features unresolved previously, and they allow for better plasma diagnostics based on these lines. Much theoretical modeling effort has been put forward to interpret these high-resolution X-ray spectra. For example, Smith et al. (2001) presented an improved collisional-radiative plasma code APEC that has been widely used in astrophysical data analysis. In addition, Behar et al. (2001) have successfully used the HULLAC atomic code (Bar-Shalom et al. 2001) to model the Capella data obtained using the high-energy transmission grating of *Chandra*. Despite those efforts in improving the atomic calculations, the need for laboratory measurements is clear: laboratory data have repeatedly shown that calculations are incomplete because they miss crucial physics left out as part of the approximations (Beiersdorfer 2003). A prime example is the significant discrepancy found between observations and code predictions, including APEC and HULLAC, in the analysis of Fe xvII and Fe xvIII line ratios (Behar et al. 2001; Xu et al. 2002). Recent laboratory measurements show that

these discrepancies, at least in the case of Fe xvII, are likely due to the accuracy of the excitation cross section of the resonance line (Beiersdorfer et al. 2004; Brown et al. 2004).

To address the need for validating the calculations using experimental data, our laboratory X-ray astrophysics program, utilizing the electron beam ion traps EBIT-I and EBIT-II at the University of California Lawrence Livermore National Laboratory, has produced large sets of reliable atomic data, including ionization and recombination cross sections for charge balance calculations, emission-line lists, excitation cross sections, and dielectronic recombination oscillator strength (for deriving rate coefficients) for interpreting X-ray line formation. An overview of this program was given by Beiersdorfer (2003). For iron, we have recently measured a complete set of Fe L-shell emission-line wavelengths (Brown et al. 1998, 2002). Various issues associated with the Fe xvII spectrum have been addressed and resolved, including opacity effects, line blending, and cross section measurements (Brown et al. 1998, 2001, 2002, 2004; Beiersdorfer et al. 2002, 2004). Moreover, Gu et al. (1999b, 2001) have reported a set of iron L-shell excitation cross sections for the L-shell lines of Fe xxI–Fe xxIV that were normalized to calculations in the high-energy limit. Although such a normalization can be fairly reliable at high electron-ion collision energies, the accuracy of electron scattering calculations is limited to 15%–30% (Zhang & Sampson 1989) and may be much worse (factors of 2 or more; see § 4), if the levels are affected by configuration interactions. A more accurate method is normalizing directly to radiative electron capture, i.e., radiative recombination (RR). This is because RR, the inverse of photoionization, is the simplest atomic scattering process at high energy involving only one electron and one photon. An RR X-ray is produced by capturing a free electron into a bound

¹ Also at Goddard Space Flight Center, Greenbelt, MD 20771.

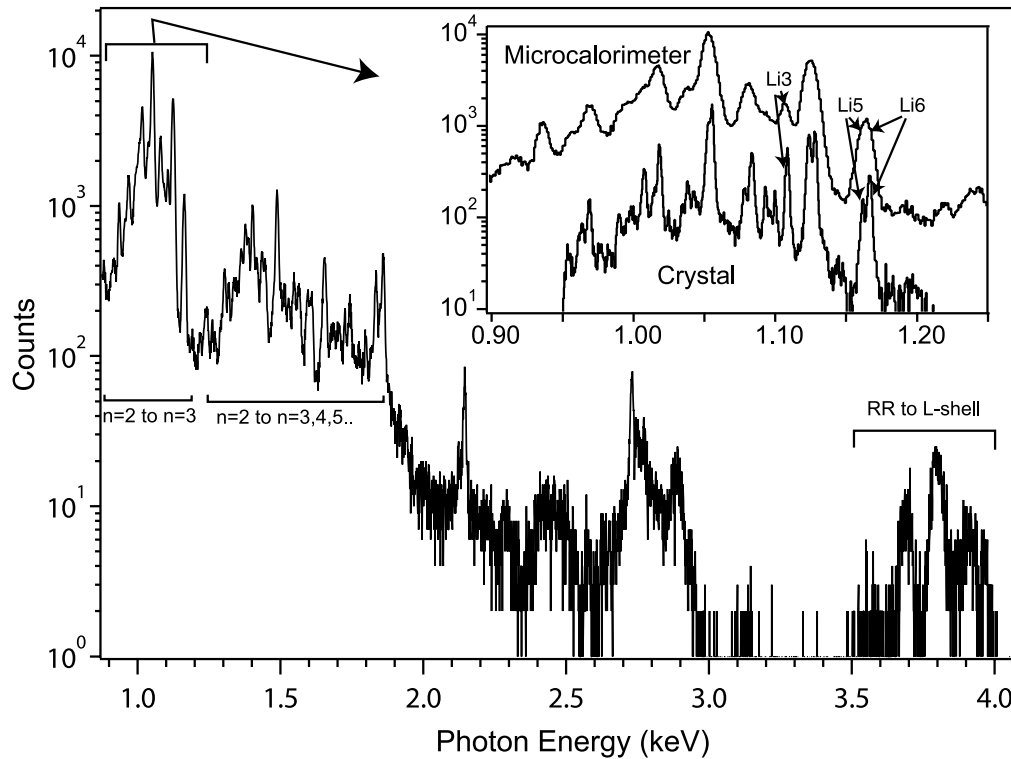


FIG. 1.—Iron spectrum taken by the XRS microcalorimeter at an electron beam energy of 2.1 keV. The inset is an enlarged view of the $3 \rightarrow 2$ lines from both the XRS and the TIAP crystal spectrometer. The line width of the L-shell lines reflects the resolution of the microcalorimeter or crystal spectrometer, while the line width of the RR lines is due to the energy distribution of the electron beam.

level. The X-ray photon has an energy equal to the sum of the free electron energy and the ionization potential of the level into which the electron is captured. At high electron energies, the RR cross sections are known from both calculations and synchrotron measurements to an accuracy of 3%–5% (Saloman et al. 1988).

The first measurement of Fe L-shell cross sections utilizing RR for normalization was reported by Chen et al. (2002). The measurement was made possible in part by the availability of a high-resolution, large-area, gain stabilized microcalorimeter, the engineering spare microcalorimeter from the original *Astro-E* satellite mission. This instrument had unique characteristics that made such measurement possible, including the ability to time-tag each X-ray event and an external duty cycle. These measurements of Chen et al. (2002) represented the first use of a calorimeter for cross section measurements. These measurements focused on selected $n = 3 \rightarrow 2$ emission lines of Fe xxiv. In this work we extend our previous measurement and report the electron impact excitation (EIE) cross sections for 17 lines from the charge states between Fe^{20+} and Fe^{23+} .

2. EXPERIMENTS

Our experiments were carried out on the EBIT-II device (Levine et al. 1988). In order to measure the Fe L-shell excitation cross section using the RR cross section as normalization, we need a detector that has a wide energy coverage to record not only the EIE (near 1 keV) but also the RR lines (at 4–5 keV in this measurement). We also need a detector that has sufficiently high energy resolution to resolve individual EIE line features. These requirements were met by using a crystal spectrometer (Beiersdorfer & Wargelin 1994; Brown et al. 1999), together with the Goddard Space Flight Center (GSFC) X-ray spectrometer (XRS) microcalorimeter detector (Kelley

et al. 1999; Stahle et al. 1999; Porter et al. 1999; Audley et al. 1999; Gendreau et al. 1999; Boyce et al. 1999). The microcalorimeter employed in our experiment was the engineering model detector from the *Astro-E* mission (Ogawara 1998). It had an energy resolution better than 10 eV and an energy coverage of about 8.5 keV (500 eV to 9 keV). The crystal spectrometer employed a flat $50 \times 25 \times 25$ mm thallium acid phthalate crystal at a 26° Bragg angle, giving a wavelength coverage from 9.5 to 12 Å (0.9–1.2 keV). It had a resolving power of 385 (FWHM of 2.6 eV at a photon energy of 1 keV). Typical Fe spectra from both instruments are shown in Figure 1. The wavelength scale was established by identifying the lines and assigning the line wavelength using references from previous experiments on EBIT-II (Brown et al. 2002) and the Princeton Large Torus tokamak (Wargelin et al. 1998). Most of the strong Fe $3 \rightarrow 2$ L-shell lines observed with the crystal spectrometer were resolved, while only a few of those observed with the microcalorimeter were resolved, illustrating the need to operate both instruments simultaneously.

The XRS has unique features that enabled the present measurements. These are a combination of high effective area (12.5 mm^2), electronic stability, and a microsecond time resolution, none of which has thus far been duplicated in other calorimeter devices. This combination is needed because the RR cross sections are about 3 orders of magnitude smaller than the electron-impact excitation cross sections. In other words, only one RR X-ray is counted for 1000 counts in a particular L-shell emission line. The microcalorimeter must thus have a large dynamic range, which in an actual measurement translates into a long-time observation without electronic gain drift.

Once- and twice-ionized iron was injected into EBIT-II using a metal vapor vacuum arc source. The ions were ionized by the beam and trapped for about 5 s. Then the trap was emptied

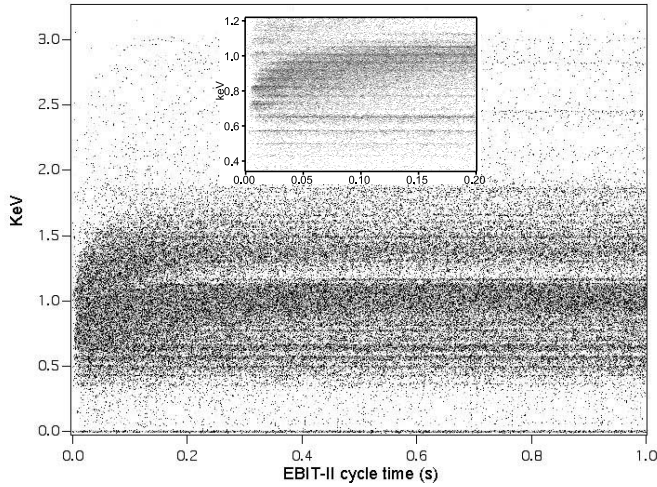


FIG. 2.—First second of XRS Fe spectrum as a function of EBIT phase time at an electron energy of 2.1 keV. The Fe was injected at 0 s. The ionizing phase lasted up to 300 ms and is indicated by a successive shift in the observed X-ray energies to higher energies, as shown in the inset for the first 200 ms. The total trapping time was 5 s.

and filled anew. During the first few hundreds of milliseconds, the injected iron undergoes a stepwise ionization until an equilibrium charge balance is reached, as shown in Figure 2. We chose to analyze only those data acquired after ionization equilibrium was reached, i.e., data recorded at least 1 s after the injection.

Our measurements were made at three electron beam energies: 2.1, 2.5, and 3.0 keV. These energies are 2–3 times higher

than the threshold for direct excitation so that we avoid contributions to the line intensities from dielectronic recombination radiation and resonance excitation. At these energies, however, cascades from higher levels may contribute to the line intensities (see § 3.3 for more details). Our method determines the effective cross section that includes all possible cascade processes at the given electron energies.

3. DATA ANALYSIS

As described in Chen et al. (2002), EIE cross sections can be derived from

$$\sigma = \frac{\sum_j G_j^{\text{RR}} \eta_j^{\text{RR}} T_j^{\text{RR}} \sigma_j^{\text{RR}}}{G \eta T} \frac{I}{I_j^{\text{RR}}}, \quad (1)$$

where σ is the total cross section for producing the line and includes cascade contributions, G represents the effects of the angular distribution of the polarized radiation, η is the efficiency of the detector, and T is the filter transmission. The summation is over the fine structure of a given ion, represented by subscript j . For example, in the case of electron capture by Li-like Fe xxiv to produce Be-like Fe xxiii, the $n = 2$ state fine structure includes $2s_{1/2}^2$ ($J = 0$), $2s_{1/2}2p_{1/2}$ ($J = 0, J = 1$), and $2s_{1/2}2p_{3/2}$ ($J = 1, J = 2$). (A complete list of the fine-structure components of the Fe L-shell RR transitions are listed in Table 1.)

It is straightforward to derive the EIE cross sections for each line if we can determine each parameter on the right-hand side of equation (1). There is, however, an extra complication in the technique. As illustrated in Figure 1, the XRS could not fully resolve the $3 \rightarrow 2$ transition lines. As a consequence, we had to rely on the crystal spectrometer to determine the individual

TABLE 1

FIT PARAMETERS FOR THE THEORETICAL TOTAL CROSS SECTION OF RR TRANSITIONS (IN UNITS OF 10^{-24} cm^2) INTO $n = 2$ STATE FINE-STRUCTURE L-SHELL LEVELS

INDEX	STRUCTURE	BINDING ENERGY (eV)	FITTING PARAMETERS					
			a	b	c	d	e	f
Fe xxiv	$2s_{1/2}J = 1/2$	2046	−11.246	256.630	120.343	−134.196	64.849	−11.477
Fe xxiv	$2p_{1/2}J = 1/2$	1997	−1.025	−1.272	342.710	−260.136	102.948	−16.196
Fe xxiv	$2p_{3/2}J = 3/2$	1981	−1.703	−7.414	670.755	−506.274	199.805	−31.397
Fe xxiii.....	$2s_{1/2}2s_{1/2}J = 0$	1951	−5.590	125.475	59.147	−68.937	33.887	−6.056
Fe xxiii.....	$2s_{1/2}2p_{1/2}J = 0$	1908	−0.207	−1.101	87.725	−65.667	25.745	−4.025
Fe xxiii.....	$2s_{1/2}2p_{1/2}J = 1$	1904	−0.607	−3.543	261.808	−195.746	76.675	−11.978
Fe xxiii.....	$2s_{1/2}2p_{3/2}J = 2$	1892	−0.849	−8.154	428.865	−319.023	124.652	−19.453
Fe xxiii.....	$2s_{1/2}2p_{3/2}J = 1$	1855	−0.566	−3.959	254.884	−190.871	74.837	−11.698
Fe xxiii.....	$2p_{1/2}2p_{1/2}J = 0$	1832	−0.023	0.629	0.583	−0.730	0.379	−0.071
Fe xxiii.....	$2p_{3/2}2p_{3/2}J = 0$	1772	−0.214	5.003	1.967	−2.545	1.296	−0.235
Fe xxii	$2p_{1/2}J = 1/2$	1800	−0.646	−7.564	363.570	−269.323	104.790	−16.295
Fe xxii	$2p_{3/2}J = 3/2$	1785	−0.944	−19.778	711.219	−523.565	203.110	−31.550
Fe xxi	$2p_{1/2}2p_{1/2}J = 0$	1688	−0.279	−3.788	166.241	−124.785	48.871	−7.629
Fe xxi	$2p_{1/2}2p_{3/2}J = 1$	1679	−0.342	−8.123	273.985	−203.701	79.257	−12.314
Fe xxi	$2p_{1/2}2p_{3/2}J = 2$	1674	−0.485	−10.634	367.592	−273.369	106.411	−16.542
Fe xxi	$2p_{3/2}2p_{3/2}J = 2$	1658	−0.119	−2.494	87.312	−65.214	25.463	−3.967
Fe xxi	$2p_{3/2}2p_{3/2}J = 0$	1637	−0.044	−0.325	19.703	−14.752	5.742	−0.890
Fe xx	$2p_{3/2}J = 3/2$	1572	−0.397	−13.749	408.734	−302.912	117.589	−18.246
Fe xx	$2p_{1/2}2p_{3/2}2p_{3/2}J = 3/2$	1554	−0.300	−8.980	277.541	−206.063	79.990	−12.401
Fe xx	$2p_{1/2}2p_{3/2}2p_{3/2}J = 1/2$	1536	−0.058	−0.970	39.130	−29.408	11.482	−1.784
Fe xx	$2p_{3/2}J = 3/2$	1529	−0.003	−0.080	2.653	−1.974	0.771	−0.120
Fe xix	$2p_{3/2}2p_{3/2}J = 2$	1454	−0.295	−12.756	358.971	−266.294	103.276	−16.008
Fe xix	$2p_{3/2}2p_{3/2}J = 0$	1444	−0.052	−2.354	64.762	−47.835	18.471	−2.852
Fe xix	$2p_{1/2}2p_{3/2}(3)J = 1$	1443	−0.084	−4.347	117.896	−87.691	34.083	−5.292
Fe xix	$2p_{1/2}2p_{3/2}(3)J = 2$	1433	0.000	−0.204	5.128	−3.917	1.555	−0.246
Fe xviii.....	$2p_{3/2}J = 3/2$	1352	−0.146	−14.267	346.643	−255.437	98.435	−15.179
Fe xviii.....	$2p_{1/2}J = 1/2$	1339	−0.006	−0.679	16.182	−11.960	4.613	−0.711

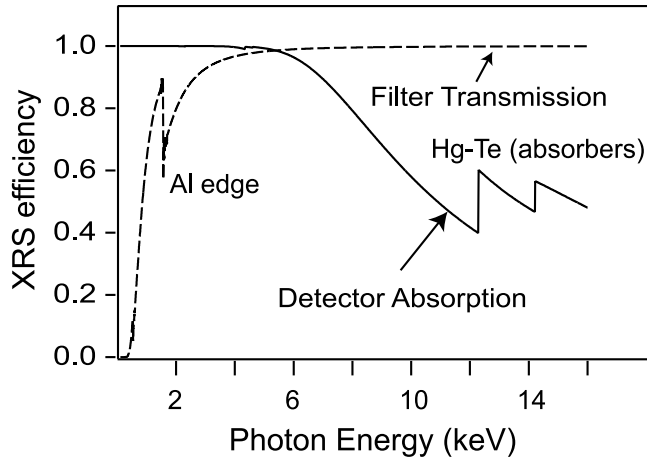


FIG. 3.—Measured transmission efficiency of the window foils and the absorption efficiency of the absorber of the XRS detector.

EIE line intensities. To do so, we need to relate the line intensities measured with the XRS to the line intensities measured with the crystal spectrometer through a geometry constant A from the two spectrometers. We have chosen two Fe xxiv lines $1s^2 3p_{1/2} \rightarrow 1s^2 2s_{1/2}$ and $1s^2 3p_{3/2} \rightarrow 1s^2 2s_{1/2}$, labeled Li5 and Li6 in Figure 1, as common references. These two lines are well isolated from the other lines, and their intensities can be determined accurately. The relation between the line intensity measured by the XRS, I_X , and the one measured by the crystal spectrometer, I_c , is

$$I_X = A \frac{G_X T_X \eta_X}{G_c T_c \eta_c} I_c. \quad (2)$$

The geometry factor A represents the ratio of the plasma volume in the field of view of the crystal and the microcalorimeter.

3.1. Effect of Polarized Radiation

Radiation from the electron beam ion trap is excited by a directional electron beam and is therefore polarized (Beiersdorfer et al. 1992; Beiersdorfer & Fujimoto 2001). The measurements

reported here were all made by viewing the ions along a line of sight perpendicular to the electron beam. For the measurement with the XRS, $G = 3/(3 - P)$ for electric-dipole transition, where P is the degree of linear polarization (Beiersdorfer et al. 1996). Here P was calculated using the Flexible Atomic Code (FAC; Gu 2003), which has very good agreement with those values calculated using the code of Zhang et al. (1990). For the crystal spectrometer, factor G includes not only the effect of the angular distribution of the polarized radiation but also the crystal reflectivity to the polarized radiation (Beiersdorfer et al. 1992, 1996; Gu et al. 1999b). For the crystal reflectivity, we used a value averaged between perfect and mosaic crystals (Henke et al. 1993). We also took into account the depolarizing effect due to a transverse beam energy of 200 eV, following the results of Beiersdorfer et al. (1996) and Gu et al. (1999a).

3.2. Detector Efficiency

The quantum efficiency of the XRS was obtained through measurements prior to the EBIT-II experiments (Gendreau et al. 1999; Audley et al. 1999). The efficiency of the XRS, shown in Figure 3, consists of foil transmission and detector quantum efficiency. The five thin-foil filters are four Al/polyimide filters (each with thickness 545/795, 498/775, 1023/1085, and 1023/1085 Å, respectively) and one 1 μm thick Be foil used to separate the XRS and EBIT-II vacua, as well as to reduce the thermal load on the XRS. During the experiment we checked the filter response to look for ice buildup and thus to account for any changes.

The efficiency of the crystal spectrometer was determined (using tabulated X-ray absorption cross sections) by taking into account the photon absorption of the window foils, including a 0.5 μm polyimide window on the spectrometer and a 1 μm polyimide window on the position-sensitive gas proportional counter. Also taken into account was the photon absorption of the P-10 (10% CH₄ and 90% Ar) gas that filled the proportional counter at 1 atmosphere pressure with a depth of 0.9 cm.

3.3. RR Cross Sections

RR cross sections for photon emission at 90° for each level j were calculated using a Hartree-Slater model (Scofield 1989, 1991) for all the Fe L-shell ions. This model has been tested,

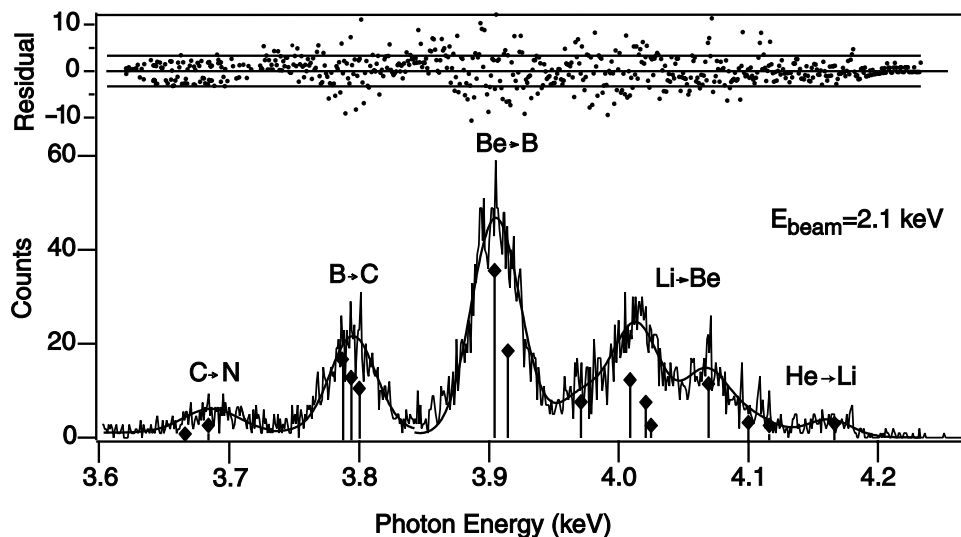


FIG. 4.—Fe RR spectrum and a spectral fit to the data at an electron beam energy of 2.1 keV. The vertical lines with diamond tops indicate the position and intensity of individual RR lines from different charge states.

TABLE 2
RELATIVE CHARGE ABUNDANCE IN THE ELECTRON BEAM ION
TRAP INFERRED FROM MICROCALORIMETER MEASUREMENTS
OF L-SHELL RADIATIVE RECOMBINATION PHOTONS

Ions	2.1 keV	2.5 keV	3.0 keV
Fe xxv	0.04	0.32	0.44
Fe xxiv	0.26	0.38	0.36
Fe xxiii	0.39	0.22	0.14
Fe xxii	0.23	0.08	0.04
Fe xxi	0.08	...	0.03

and its results have been found to be in good agreement with photoionization experiments (Saloman et al. 1988). From the energy of the levels and the electron beam energy we can determine the position of the RR line, and from the cross sections we can determine the relative intensity of the lines within one charge state: $I^{\text{RR}} \propto n_i \sigma_j^{\text{RR}} v_e$. As a matter of fact, the accurate knowledge of the energy (position) and relative intensity (amplitude) of each RR line provides tight constraints on the RR line intensity fitting (see § 3.4) and therefore results in an accurate RR line intensity analysis.

To present the theoretical RR cross sections (in units of 10^{-24} cm^2), we made a fit to the data at electron energies (in keV) ranging between 0.5 and 10 keV, using a fifth-order polynomial fit in $1/E$: $\sigma = a(1/E)^0 + b(1/E)^1 + c(1/E)^2 + d(1/E)^3 + e(1/E)^4 + f(1/E)^5$. The fitting parameters are listed in Table 1.

3.4. RR Line Intensity

The RR spectrum for an electron beam energy of 2.1 keV measured by the XRS microcalorimeter is shown in Figure 4. The RR X-rays were produced by the capture of beam electrons, thereby populating various fine-structure levels of the $n = 2$ states of Fe^{20+} through Fe^{23+} ions. Unlike in a Maxwellian plasma, RR X-rays excited by a nearly monoenergetic

electron beam form distinct, resolved features whose width is determined by the energy distribution of the electron beam. From the data we determine the energy spread of the electron beam to be $40 \pm 2 \text{ eV}$ for the 2.1 keV electron beam and $44 \pm 3 \text{ eV}$ for the 3.0 keV beam. This width is larger than the fine-structure separations of the individual RR lines. These separations are as small as 10 eV (see Fig. 4, where the individual RR lines are indicated by vertical lines); consequently, we cannot resolve them in the XRS spectrum despite the good resolving power of the microcalorimeter. However, the separations of the RR features among different charge states are typically more than twice the electron beam energy width and can be distinguished clearly in the XRS spectrum.

The parameter I^{RR} is determined by fitting the RR emission using the position and relative intensities of each RR fine-structure configuration known from theory (see Table 1). We achieved very reliable spectral fits for the RR spectra at all three beam energies.

It is interesting to note that we have different charge balances in the trap at these three electron energies, and this information can be extracted from the RR intensities. We can infer the ionization balance from spectral fits to the RR data using Chen et al. (2002):

$$n_i \propto \frac{I^{\text{RR}}}{\sum_j G_j^{\text{RR}} \eta_j^{\text{RR}} T_j^{\text{RR}} \sigma_j^{\text{RR}}}. \quad (3)$$

The results for the beam energies of 2.1, 2.5, and 3.0 keV are in Table 2. The dominant ion in the trap was Fe xxiii at an electron beam energy of 2.1 keV, while Fe xxiv and Fe xxv ions became dominant at an electron beam energy of 3.0 keV. This charge balance information was used for the excitation line-fitting process as described in the next section.

3.5. EIE Line Intensity

The complexity of the Fe L-shell spectrum requires a line-fitting procedure that takes into account all possible lines,

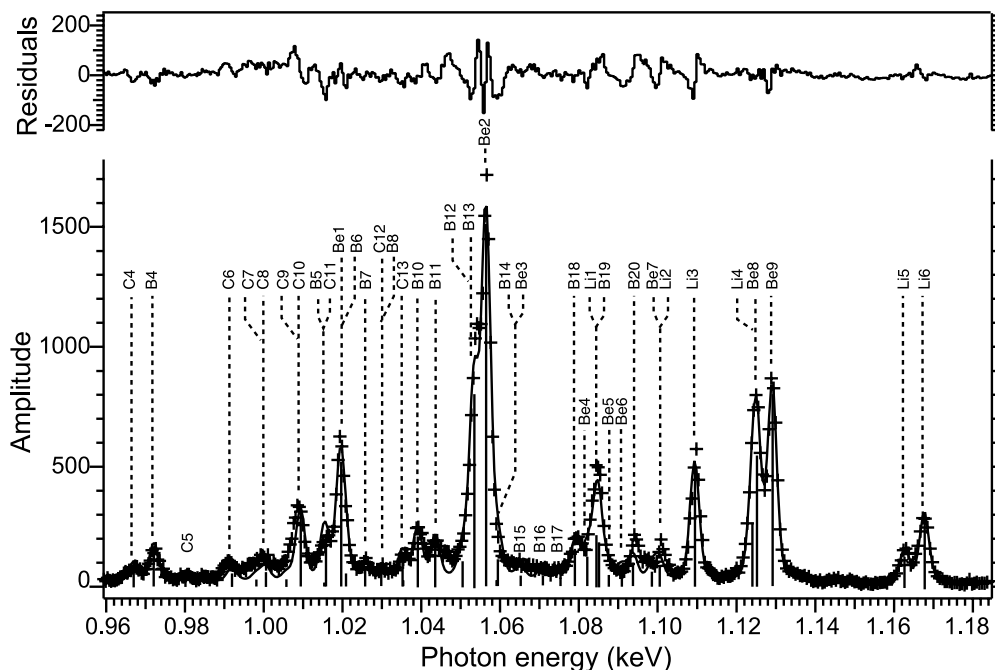


Fig. 5.—Fe crystal spectrum and its fit at an electron energy of 2.1 keV. The lines are labeled with notation by Brown et al. (2002); the transitions are listed in Table 3.

TABLE 3
EMISSION-LINE WAVELENGTH AND RELATIVE INTENSITY FROM BROWN ET AL. (2002) USED IN THE EIE FITTING PROGRAM

Label	Atomic Transition	Wavelength (Å)	Energy (keV)	Relative Intensity
C4.....	$1s^2 2s_{1/2} 2p_{1/2} 2p_{3/2} 3d_{5/2} (J=2) \rightarrow 1s^2 2s_{1/2} 2p^2 2p_{3/2} (J=1)$	12.822	0.967	0.5
C5.....	$1s^2 2s_{1/2} 2p_{1/2} 2p_{3/2} 3d_{5/2} (J=2) \rightarrow 1s^2 2s_{1/2} 2p_{1/2} 2p^2_{3/2} (J=1)$	12.649	0.980	0.1
C6.....	$1s^2 2s^2 2p_{1/2} 3d_{5/2} (J=3) \rightarrow 1s^2 2s^2 2p_{1/2} 2p_{3/2} (J=2)$	12.499	0.992	0.2
C7.....	$1s^2 2s^2 2p_{1/2} 3d_{5/2} (J=2) \rightarrow 1s^2 2s^2 2p_{1/2} 2p_{3/2} (J=1)$	12.422	0.998	0.1
C8.....	$1s^2 2s^2 2p_{1/2} 3d_{3/2} (J=1) \rightarrow 1s^2 2s^2 2p_{1/2} 2p_{3/2} (J=1)$	12.393	1.000	0.2
C9.....	$1s^2 2s^2 2p_{3/2} 3d_{5/2} (J=2, 3) \rightarrow 1s^2 2s^2 2p_{1/2} 2p_{3/2} (J=2)$	12.327	1.006	0.1
C10.....	$1s^2 2s^2 2p_{1/2} 3d_{3/2} (J=1) \rightarrow 1s^2 2s^2 2p^2 (J=0)$	12.284	1.009	1
C11.....	$1s^2 2s_{1/2} 2p_{1/2} 2p_{3/2} 3d_{3/2} (J=2) \rightarrow 1s^2 2s_{1/2} 2p^2_{1/2} 2p_{3/2} (J=1)$	12.204	1.016	0.1
C12.....	$1s^2 2s_{1/2} 2p_{1/2} 2p_{3/2} 3p_{3/2} (J=1) \rightarrow 1s^2 2s^2 2p_{1/2} 2p_{3/2} (J=1)$	12.044	1.029	0.05
C13.....	$1s^2 2s_{1/2} 2p^2 3p_{3/2} (J=1) \rightarrow 1s^2 2s^2 2p^2 (J=0)$	11.975	1.035	0.1
B4.....	$1s^2 2s_{1/2} 2p_{1/2} 3s_{1/2} (J=1/2) \rightarrow 1s^2 2s_{1/2} 2p_{1/2} 2p_{3/2} (J=3/2)$	12.754	0.972	0.3
B5.....	$1s^2 2s_{1/2} 2p_{1/2} 3d_{5/2} \rightarrow 1s^2 2s_{1/2} 2p_{1/2} 2p_{3/2} (J=3/2)$	12.210	1.015	0.4
B6.....	$1s^2 2s_{1/2} 2p_{3/2} 3d_{5/2} \rightarrow 1s^2 2s_{1/2} 2p_{1/2} 2p_{3/2} (J=5/2)$	12.144	1.021	0.1
	$1s^2 2s_{1/2} 2p_{3/2} 3d_{5/2} \rightarrow 1s^2 2s_{1/2} 2p_{1/2} 2p_{3/2} (J=3/2)$			
B7.....	$1s^2 2s_{1/2} 2p_{3/2} 3d_{5/2} \rightarrow 1s^2 2s_{1/2} 2p^2_{3/2} (J=3/2)$	12.089	1.026	0.1
B8.....	$1s^2 2s_{1/2} 2p_{3/2} 3d_{3/2} \rightarrow 1s^2 2s_{1/2} 2p^2_{3/2} (J=3/2)$	12.038	1.030	0.1
B9.....	$1s^2 2s^2 3d_{3/2} (J=3/2) \rightarrow 1s^2 2s^2 2p_{3/2} (J=3/2)$	11.977	1.035	0.2
B10.....	$1s^2 2s^2 3d_{5/2} (J=5/2) \rightarrow 1s^2 2s^2 2p_{3/2} (J=3/2)$	11.932	1.039	0.4
B11.....	$1s^2 2s_{1/2} 2p_{1/2} 3d_{5/2} (J=5/2) \rightarrow 1s^2 2s_{1/2} 2p_{1/2} 2p_{3/2} (J=3/2)$	11.881	1.044	0.2
B12.....	$1s^2 2s_{1/2} 2p_{1/2} 3d_{5/2} (J=5/2) \rightarrow 1s^2 2s_{1/2} 2p_{1/2} 2p_{3/2} (J=3/2)$	11.802	1.051	0.2
B12.....	$1s^2 2s_{1/2} 2p_{3/2} 3d_{3/2} (J=3/2) \rightarrow 1s^2 2s_{1/2} 2p^2 (J=1/2)$			
B13.....	$1s^2 2s^2 3d_{3/2} (J=3/2) \rightarrow 1s^2 2s^2 2p_{1/2} (J=1/2)$	11.770	1.053	1
B14.....	$1s^2 2s_{1/2} 2p_{1/2} 3p_{3/2} (J=3/2) \rightarrow 1s^2 2s^2 2p_{3/2} (J=3/2)$	11.704	1.059	0.05
B15.....	$1s^2 2s_{1/2} 2p_{1/2} 3p_{1/2} (J=1/2) \rightarrow 1s^2 2s^2 2p_{1/2} (J=1/2)$	11.640	1.065	0.05
B16.....	$1s^2 2s_{1/2} 2p_{1/2} 3p_{1/2} (J=1/2) \rightarrow 1s^2 2s^2 2p_{1/2} (J=1/2)$	11.578	1.071	0.05
B17.....	$1s^2 2s_{1/2} 2p_{3/2} 3p_{1/2} (J=1/2) \rightarrow 1s^2 2s^2 2p_{3/2} (J=3/2)$	11.530	1.075	0.05
B18.....	$1s^2 2s_{1/2} 2p_{1/2} 3p_{3/2} (J=3/2) \rightarrow 1s^2 2s^2 2p_{1/2} (J=1/2)$	11.490	1.079	0.2
B19.....	$1s^2 2s_{1/2} 2p_{1/2} 3p_{3/2} (J=3/2) \rightarrow 1s^2 2s^2 2p_{1/2} (J=1/2)$	11.427	1.085	0.2
B20.....	$1s^2 2s_{1/2} 2p_{3/2} 3p_{3/2} (J=3/2) \rightarrow 1s^2 2s^2 2p_{3/2} (J=3/2)$	11.400	1.088	0.05
Be1.....	$1s^2 2s_{1/2} 3s_{1/2} (J=0) \rightarrow 1s^2 2s_{1/2} 2p_{3/2} (J=1)$	12.161	1.020	0.3
Be2.....	$1s^2 2s_{1/2} 3d_{5/2} (J=2) \rightarrow 1s^2 2s_{1/2} 2p_{3/2} (J=1)$	11.736	1.056	1
Be3.....	$1s^2 2s_{1/2} 3s_{1/2} (J=1) \rightarrow 1s^2 2s_{1/2} 2p_{1/2} (J=1)$	11.702	1.060	0.1
Be3.....	$1s^2 2p_{1/2} 3d_{5/2} (J=3) \rightarrow 1s^2 2p_{1/2} 2p_{3/2} (J=2)$			
Be4.....	$1s^2 2s_{1/2} 3d_{5/2} (J=3) \rightarrow 1s^2 2s_{1/2} 2p_{3/2} (J=2)$	11.458	1.082	0.07
Be5.....	$1s^2 2s_{1/2} 3d_{3/2} (J=1) \rightarrow 1s^2 2s_{1/2} 2p_{1/2} (J=1)$	11.366	1.091	0.05
Be6.....	$1s^2 2s_{1/2} 3d_{3/2} (J=2) \rightarrow 1s^2 2s_{1/2} 2p_{1/2} (J=1)$	11.336	1.094	0.05
Be7.....	$1s^2 2s_{1/2} 3d_{3/2} (J=1) \rightarrow 1s^2 2s_{1/2} 2p_{1/2} (J=0)$	11.285	1.099	0.05
Be8.....	$1s^2 2s_{1/2} 3p_{1/2} (J=1) \rightarrow 1s^2 2s^2 (J=0)$	11.019	1.125	0.39
Be9.....	$1s^2 2s_{1/2} 3p_{3/2} (J=1) \rightarrow 1s^2 2s^2 (J=0)$	10.981	1.129	0.6
Li1.....	$1s^2 3s_{1/2} (J=1/2) \rightarrow 1s^2 2p_{3/2} (J=3/2)$	11.432	1.085	0.4
Li2.....	$1s^2 3s_{1/2} (J=1/2) \rightarrow 1s^2 2p_{1/2} (J=1/2)$	11.266	1.101	0.15
Li3.....	$1s^2 3d_{5/2} (J=5/2) \rightarrow 1s^2 2p_{3/2} (J=3/2)$	11.176	1.109	1
Li4.....	$1s^2 3d_{3/2} (J=3/2) \rightarrow 1s^2 2p_{1/2} (J=1/2)$	11.029	1.124	0.5
Li5.....	$1s^2 3p_{1/2} (J=1/2) \rightarrow 1s^2 2s_{1/2} (J=1/2)$	10.663	1.163	0.4
Li6.....	$1s^2 3p_{3/2} (J=3/2) \rightarrow 1s^2 2s_{1/2} (J=1/2)$	10.618	1.168	0.8

because many weak lines could have a nonnegligible contribution to the intensity of strong lines. To account for all possible line features, we constructed a model utilizing the data from the Fe L-shell line survey (Brown et al. 2002). The model includes all observed L-shell emission lines with measured wavelengths and relative intensities at all charge states. From the charge balance obtained through the RR line fitting (Table 2), we derived initial amplitudes for each line using the available relative intensities of lines from each individual charge state (Brown et al. 2002). During fitting, we allowed the relative intensity to vary within 30% to account for unmeasured factors such as polarization effects and intensity changes at different electron beam energies. The position of the lines was fixed. The line shape was fitted by a Voigt profile, which is a convolution of a Lorentzian and Gaussian function. The line width was set to be

the same for all the lines. This information provided us with a constraint similar to that of the RR line fitting discussed above. As is shown in Figure 5, we achieved good fits to the measured spectra using this constrained method.

We noticed that the fitting of a couple of lines could be improved if we set the line wavelength as a free parameter. For example, the intensity of the C-like Fe xxii line C10 would increase 10%–30% if its wavelength were allowed to vary from 12.284 Å (1.009 keV) up to 12.312 Å (1.007 keV). Such a wavelength variation, however, would be inconsistent with the data (12.284 ± 0.002 Å) from the wavelength survey (Brown et al. 2002). Moreover, there is a possibility that the few lines that appear to be imperfectly fitted could be blended by unidentified weak lines. We note that even a change of 30% would not remove the extreme discrepancies between some

TABLE 4

RESULTS OF EXCITATION CROSS SECTIONS (IN UNITS OF 10^{-21} cm^2) AT THREE ELECTRON BEAM ENERGIES FROM THIS EXPERIMENT AND TWO THEORETICAL MODELS

LINE	2.1 keV			2.5 keV			3.0 keV		
	Measurement	FAC	HULLAC	Measurement	FAC	HULLAC	Measurement	FAC	HULLAC
C4.....	5.7 ± 1.0	4.9					7.1 ± 2.9	4.2	
C8.....	4.3 ± 0.9	5.6					4 ± 1.5	4.9	
C10.....	16.3 ± 3.3	32.3	32.9				11.2 ± 3.2	28.6	32
B6.....	2.5 ± 0.6	1.9		2.3 ± 0.8	1.8		2.3 ± 0.6	1.6	
B10.....	4.4 ± 0.8	5.2					4.2 ± 0.8	3.9	
B13.....	15.9 ± 2.5	17.4	17.8	11.5 ± 2.1	16.2	17.2	13.9 ± 2.3	15	16
B19.....	3.4 ± 0.6	3.2	4.1	2.6 ± 0.6	3.2	3.6	3.6 ± 0.7	3.1	3.4
Be1.....	6.4 ± 0.6	8.7	8.6	5.7 ± 0.8	7.6	7.1	5.1 ± 0.6	6.6	6.1
Be2.....	15.8 ± 1.4	15.7	15.9	11.4 ± 1.6	14.7	14.1	12.8 ± 1.5	13.4	13.1
Be4.....	1.2 ± 0.2	1.6		0.8 ± 0.2	1		0.8 ± 0.1	0.6	
Be8.....	4.4 ± 0.4	4.3	4.3	4.1 ± 0.6	4.1	4.1	4.2 ± 0.5	4	4.2
Be9.....	6.4 ± 0.6	6.6	6.4	6.2 ± 0.9	6.6	6.1	6.8 ± 0.8	6.4	6.4
Li1.....	3.4 ± 0.3	3.4	3.3	2.7 ± 0.4	2.9	2.6	2.3 ± 0.2	2.5	2.2
Li3.....	7.1 ± 0.6	6.4	6.8	5.2 ± 0.6	5.6	5.7	5.3 ± 0.5	4.9	5.2
Li3 ^a	6.3 ± 0.6			4.5 ± 0.9			5.0 ± 0.5		
Li4.....	3.7 ± 0.3	3.6	3.4	3 ± 0.4	3.1	3	2.9 ± 0.3	2.7	2.8
Li5.....	1.8 ± 0.2	2.4	2.3	2 ± 0.3	2.3	2	2.1 ± 0.2	2.1	2.1
Li5 ^a	1.8 ± 0.2			1.8 ± 0.4			2.1 ± 0.2		
Li6.....	3.5 ± 0.3	4.5	4	4.1 ± 0.5	4.3	3.9	3.6 ± 0.4	4.1	3.7
Li6 ^a	3.1 ± 0.4			3.4 ± 0.7			3.4 ± 0.3		

^a Measurements from Chen et al. (2002).

experimental and theoretical results, as discussed below. The data used for the EIE fitting are summarized in Table 3, where the line labels, transition energies, and relative line intensities are taken from Brown et al. (2002).

4. RESULTS AND DISCUSSIONS

The results of the EIE cross section measurements for the lines from Fe xxI to Fe xxIV are summarized in Table 4. The quoted uncertainties are equivalent to a 1σ statistical confidence level, and they include the statistical fitting error of the line intensities as well as uncertainties in filter transmissions and detector responses for both the crystal spectrometer and the microcalorimeter. We also estimated the errors associated with accounting for the angular distribution correction and crystal reflectivities. An additional error comes from determining the appropriate intensity of the background level, given the high density of the unresolved weak iron lines in the XRS spectra. In the analysis, we estimated the upper and lower limit of the background level to assess this error. The total error given is from the quadrature summation of all individual errors.

In Table 4 the EIE cross sections from the present measurement are compared with the theoretical values of the EIE cross sections from calculations utilizing the codes FAC (Gu 2003) and HULLAC (Bar-Shalom et al. 2001). A graphical comparison for selected lines is shown in Figure 6. At the present electron energies, levels higher than $n = 3$ can be excited, and cascades from such higher n -levels contribute to the observed line intensities. Cascades from levels up to $n = 12$ are included in the FAC calculations and up to $n = 6$ in the HULLAC calculations. Overall, the cascade contribution accounts for 4%–52% of the total line intensities, as shown in Table 5. We expect cascade contributions from $n > 12$ to be negligible.

Our measurements show that the calculations are in good agreement with many of the measurements for B-like, Be-like, and Li-like lines. This indicates that the calculations are quite

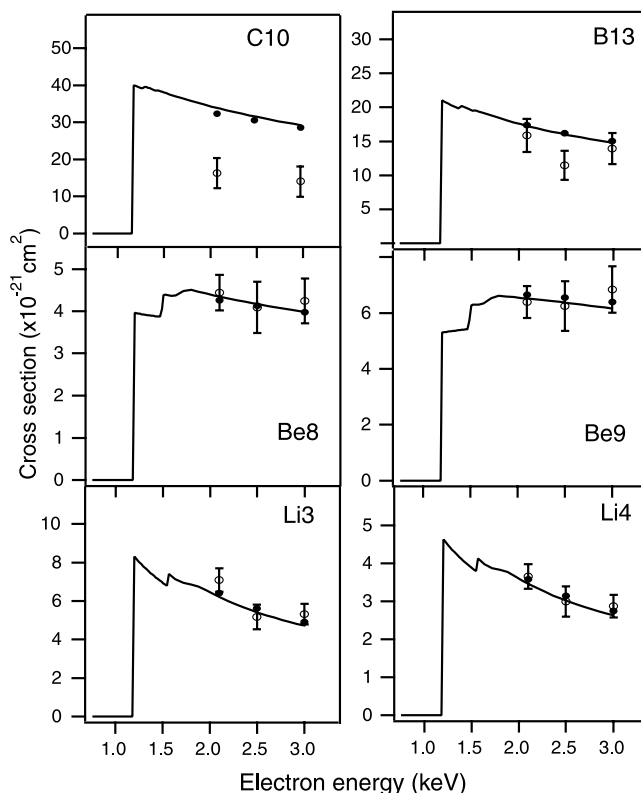


FIG. 6.—Selected, measured, effective excitation cross sections (open circles with error bars) for lines from four different charge states and comparison with theoretical calculations using the codes HULLAC (lines) and FAC (solid circles).

TABLE 5
CALCULATED CASCADE CONTRIBUTION TO THE LINE
INTENSITY AT AN ELECTRON COLLISION ENERGY
OF 2.4 keV USING CODE FAC

Line	Fraction
C4.....	0.09
C8.....	0.11
C10.....	0.04
B6.....	0.36
B10.....	0.25
B13.....	0.05
B19.....	0.18
Be1.....	0.05
Be2.....	0.09
Be4.....	0.52
Be8.....	0.17
Be9.....	0.19
Li1.....	0.11
Li3.....	0.13
Li4.....	0.14
Li5.....	0.18
Li6.....	0.19

accurate in many cases. However, some significant discrepancies exist.

First, the measured cross sections for the Li5 and Li6 lines are slightly lower than those calculated, particularly at the electron energy of 2.1 keV. These observations are consistent with our previous measurements for those lines (Chen et al. 2002) where the measured cross sections were somewhat lower compared to *R*-matrix calculations. The physical cause of this discrepancy is not clear. We note that cascades from levels up to $n = 12$ have been taken into account in our calculations. However, cascades will only add to the theoretical value, which is already larger than the measurement. The differences between our measurements and calculations are largest at the lowest energy. While the calculated cross sections diminish with electron energy, the measured cross sections for Li5 and Li6 seem rather constant. By contrast, the measured cross sections for Li1, Li3, and Li4 decrease with electron energy as predicted by the calculations.

Second, the calculated cross section of the Be-like Fe xxii line Be1 also appears to be somewhat larger than the measurement. For example, the measured value is $(6.4 \pm 0.6) \times 10^{-21} \text{ cm}^2$ at the 2.1 keV electron energy, which is about 25% less than the calculated values of $8.7 \times 10^{-21} \text{ cm}^2$ (FAC) and $8.6 \times 10^{-21} \text{ cm}^2$ (HULLAC). This line (Be1) is blended with the B6 line B-like Fe xxii (Brown et al. 2002); therefore, we might have incorrectly accounted for the line blend, although

we have used the tightest available constraints. Indeed, our results for line B6, which was identified with two transitions (see Table 3), are somewhat larger than the calculated values, albeit the discrepancy is within the uncertainty limit of the measurement. If some intensity of line B6 was assigned to Be1 (see Fig. 5), it would bring the measured cross section of Be1 up about 15%—this is still not in very good agreement with the calculations. A similarly blended line pair is formed by lines B13 and Be2. Here good agreement is found between measurement and calculation. We note that line Fe xxii B13 [$1s^2 2s^2 3d_{3/2} (J = 3/2) \rightarrow 1s^2 2s^2 2p_{1/2} (J = 1/2)$] is sensitive to the plasma density (Wargelin et al. 1998; Chen et al. 2004). Although this property could potentially affect the measurement, it was not the case in our measurements. At densities between 1×10^{10} and $5 \times 10^{12} \text{ cm}^{-3}$, the EBIT-II source is at the low-density limit for this line.

Third, the relatively small population of C-like ions in the trap resulted in larger uncertainties in the measurements for C-like lines than for the lines of the other charge states. The increased uncertainties, however, cannot explain the large discrepancy (almost a factor of 2) between measurement and theory for the strongest line, Fe xxii C10. As discussed before, the intensity of this line could be increased by up to 30% if we allowed its wavelength to be a variable in our fit. Such a relaxation of the fit constraints is not enough to reduce the large observed discrepancy and would not resolve the discrepancy. One possible explanation is the density sensitivity of this line $1s^2 2s^2 2p_{1/2} 3d_{3/2} (J = 1) \rightarrow 1s^2 2s^2 2p^2 (J = 0)$, which starts at densities of about 10^{11} – 10^{12} cm^{-3} (Phillips et al. 1996). At these densities, which are close to those estimated for our machine, the population in the $n = 2$ state fine-structure levels $1s^2 2s^2 2p^2 J = 1$ and $J = 2$ become sufficiently high that the excitation from the ground level $J = 0$ will be reduced, resulting in a lower measured cross section.

We expect that further measurements and improved modeling will eventually resolve the discrepancies noted for the few lines in Fe xxii, Fe xxiii, and Fe xxiv. Until these discrepancies are resolved, we recommend not using these lines for determining abundances and other parameters when analyzing astrophysical spectra, especially when other lines from these ionization stages are available for diagnostic purposes.

This work was performed under the auspices of the US Department of Energy by the University of California-Livermore National Laboratory under contract W-7405-Eng-48 and supported by NASA Astronomy and Physics Research and Analysis grants to LLNL, GSFC, and Stanford University.

REFERENCES

- Audley, M. D., et al. 1999, *Proc. SPIE*, 3765, 751
 Bar-Shalom, A., Klapisch, M., & Oreg, J. 2001, *J. Quant. Spectrosc. Radiat. Transfer*, 71, 169
 Behar, E., Cottam, J., & Kahn, S. M. 2001, *ApJ*, 548, 966
 Beiersdorfer, P. 2003, *ARA&A*, 41, 343
 Beiersdorfer, P., & Fujimoto, T. 2001, LLNL Rep. UCRL-ID-146907
 Beiersdorfer, P., Phillips, T. W., Wong, K. L., Marrs, R. E., & Vogel, D. A. 1992, *Phys. Rev. A*, 46, 3812
 Beiersdorfer, P., & Wargelin, B. J. 1994, *Rev. Sci. Instrum.*, 65, 13
 Beiersdorfer, P., et al. 1996, *Phys. Rev. A*, 53, 3974
 ———. 2002, *ApJ*, 576, L169
 ———. 2004, *ApJ*, 610, 616
 Boyce, K. R., et al. 1999, *Proc. SPIE*, 3765, 741
 Brown, G. V., Beiersdorfer, P., Chen, H., Chen, M. H., & Reed, K. J. 2001, *ApJ*, 557, L75
 Brown, G. V., Beiersdorfer, P., Liedahl, D. A., Widmann, K., & Kahn, S. M. 1998, *ApJ*, 502, 1015
 Brown, G. V., Beiersdorfer, P., Liedahl, D. A., Widmann, K., Kahn, S. M., & Clothiaux, E. J. 2002, *ApJS*, 140, 589
 Brown, G. V., Beiersdorfer, P., & Widmann, K. 1999, *Rev. Sci. Instrum.*, 70, 280
 Brown, G. V., et al. 2004, *Phys. Rev. Lett.*, submitted
 Chen, H., Beiersdorfer, P., Heeter, L. A., Liedahl, D. A., Naranjo-Rivera, K. L., Träbert, E., Gu, M. F., & Lepson, J. K. 2004, *ApJ*, 611, 598
 Chen, H., et al. 2002, *ApJ*, 567, L169
 Gendreau, K. C., et al. 1999, *Proc. SPIE*, 3765, 137
 Gu, M. F. 2003, *ApJ*, 582, 1241
 Gu, M. F., Kahn, S. M., Savin, D. W., Bahar, E., Beiersdorfer, P., Brown, G. V., Liedahl, D. A., & Reed, K. 2001, *ApJ*, 563, 462
 Gu, M. F., Savin, D. W., & Beiersdorfer, P. 1999a, *J. Phys. B*, 32, 5371

- Gu, M. F., et al. 1999b, *ApJ*, 518, 1002
- Henke, B. L., Gullikson, E. M., & Davis, J. C. 1993, *At. Data Nucl. Data Tables*, 54, 181
- Kahn, S. M., & Liedahl, D. A. 1990, in *Iron Line Diagnostics in X-Ray Sources*, ed. A. Treves, G. C. Perola, & L. Stella (Berlin: Springer), 3
- Kelley, R. L., et al. 1999, *Proc. SPIE*, 3765, 114
- Levine, M. A., Marrs, R. E., Henderson, J. R., Knapp, D. A., & Schneider, M. B. 1988, *Phys. Scr.*, 22, 157
- Ogawara, Y. 1998, in *IAU Symp. 188, The Hot Universe*, ed. K. Koyama, S. Kitamoto, & M. Itoh (Dordrecht: Kluwer), 75
- Paerels, F. B. S., & Kahn, S. M. 2003, *ARA&A*, 41, 291
- Phillips, K. J. H., Bhatia, A. K., Mason, H. E., & Zarro, D. M. 1996, *ApJ*, 466, 549
- Porter, F. S., et al. 1999, *Proc. SPIE*, 3765, 729
- Saloman, E. B., Hubbell, J. H., & Scofield, J. H. 1988, *At. Data Nucl. Data Tables*, 38, 1
- Scofield, J. H. 1989, *Phys. Rev. A*, 40, 3054
- . 1991, *Phys. Rev. A*, 44, 139
- Smith, R. K., Brickhouse, N. S., Liedahl, D. A., & Raymond, J. C. 2001, *ApJ*, 556, L91
- Stahle, C. K., et al. 1999, *Proc. SPIE*, 3765, 82
- Wargelin, B. J., Beiersdorfer, P., Liedahl, D. A., Kahn, S. M., & von Goeler, S. 1998, *ApJ*, 496, 1031
- Xu, H., et al. 2002, *ApJ*, 579, 600
- Zhang, H. L., & Sampson, D. H. 1989, *At. Data Nucl. Data Tables*, 43, 1
- Zhang, H. L., Sampson, D. H., & Clark, R. E. H. 1990, *Phys. Rev. A*, 41, 198